Computational analysis of the tether-pulling experiment to probe plasma membrane-cytoskeleton interaction in cells

Kristopher R. Schumacher,[1] Aleksander S. Popel,[1] Bahman Anvari,[2] William E. Brownell,[3] and Alexander A. Spector[1],*

[1]*Department of Biomedical Engineering, Johns Hopkins University, Baltimore, Maryland 21205, USA*

[2]*Department of Bioengineering, University of California–Riverside, Riverside, California 92521, USA*

[3]*Bobby R. Alford Department of Otolaryngology–Head and Neck Surgery, Baylor College of Medicine, Houston, Texas 77030, USA*

Tethers are thin membrane tubes that can be formed when relatively small and localized forces are applied to cellular membranes and lipid bilayers. Tether pulling experiments have been used to better understand the fine membrane properties. These include the interaction between the plasma membrane and the underlying cytoskeleton, which is an important factor affecting membrane mechanics. We use a computational method aimed at the interpretation and design of tether pulling experiments in cells with a strong membrane-cytoskeleton attachment. In our model, we take into account the detailed information in the topology of bonds connecting the plasma membrane and the cytoskeleton. We compute the force-dependent piecewise membrane deflection and bending as well as modes of stored energy in three major regions of the system: body of the tether, membrane-cytoskeleton attachment zone, and the transition zone between the two. We apply our method to three cells: cochlear outer hair cells (OHCs), human embryonic kidney (HEK) cells, and Chinese hamster ovary (CHO) cells. OHCs have a special system of pillars connecting the membrane and the cytoskeleton, and HEK and CHO cells have the membrane-cytoskeleton adhesion arrangement via bonds (e.g., PIP2), which is common to many other cells. We also present a validation of our model by using experimental data on CHO and HEK cells. The proposed method can be an effective tool in the analyses of experiments to probe the properties of cellular membranes.

I. INTRODUCTION

If a point force of sufficient magnitude is applied to the plasma membrane of a cell, a long thin membranous tube, i.e., a tether, forms. Tethers are formed naturally in various biological situations such as leukocyte rolling, but have also been generated experimentally to investigate the properties of biomembranes. The first reported observation of a membrane tether formed from a biological cell is associated with a red blood cell (RBC) attached to a solid surface and exposed to shear flow [1]. In fact, the RBC, whose membrane and cytoskeleton structure and properties are well characterized, has been the subject of numerous tether experiments. Later, the microchamber technique was devised as a more accurate way to study the tether formation process [2]. More recently, measurements of the forces involved in tether formation and extension have been accurately obtained using optical tweezers, magnetic tweezers, and atomic force microscopy techniques. In the optical tweezers setup, an ~5 μm diameter microbead, capable of exerting forces of several hundreds of pN, is used to extrude the membrane tether [3,4]. The magnetic bead variant and the atomic force microscope cantilever variants can apply thousands of pN [5]. Regardless of the particular mode of pulling a tether, the general idea in tether formation is to apply a force over a small area of the cell's membrane surface. The force exerted is recorded during the experiment and used to provide information on the mechanical properties of the cell. Once the tether is formed, it can be held at a constant force and the system will equilibrate.

In order to provide further interpretation to the tether pulling experiments, thermodynamic-based theoretical relationships were developed that correlate the main variables of the problem (e.g., bending modulus, far-field membrane tension, and adhesion energy) to experimentally measurable quantities (e.g., holding force and tether radius) [6,7]. These theoretical relationships in conjunction with experimental data have proved to be very useful in providing estimates of the mechanical properties of plasma membranes. For example, the theory has been applied to determine: the bending modulus of giant unilamellar vesicles [2,8], red blood cells [6], and neuronal growth cones [7], the characteristics of membrane adhesion to the cytoskeleton in red blood cells [9,10], neutrophils [11], and fibroblasts [12], the nonlocal bending modulus in giant vesicles [13,14], and the membrane viscosity in neutrophils [15], neuronal growth cones [7], and other cells [16].

In some biological systems, e.g., the cochlear outer hair cell (OHC), the human embryonic kidney (HEK) cell, and the Chinese hamster ovary (CHO) cell, the membrane exhibits significant bonding to the underlying cytoskeleton. In the OHC, the membrane is attached to cytoskeletal actin filaments via an array of pillars of unknown composition. For HEK and CHO cells, the membrane-cytoskeleton connection is probably like many other cells where, in addition to intramembrane proteins bonding, the membrane is connected to cytoskeletal actin filaments via phosphatidylinositol bisphosphate (PIP2) bonding [17,12,18]. Thus, the bonding in HEK and CHO cells is different than in OHCs. In the thermodynamic approach, the membrane-cytoskeleton interaction is characterized by a single constant, the adhesion energy. In reality, such interaction depends on a number of

*Corresponding author; aspector@jhu.edu

structural and mechanical parameters and it is a function of spatial coordinates. Knowledge of all regions of the membrane's shape after the application of the tether force is important for a further understanding of the mechanics of these cells, including, *inter alia*, an analysis of stress and energy distributions along the surface of the membrane.

Interestingly, these three cells, OHC, HEK, and CHO, are important in studies of the membrane protein, prestin, critical to mammalian active hearing [19,20]. The OHC is the cell native to prestin where it is a key part of the motor complex responsible for the generation of active force and energy. The properties of this cell's composite wall, including the membrane and cytoskeleton have previously been studied using various experimental [21,22] and modeling [23–27] techniques. HEK and CHO cells have been used for prestin transfection, and provided information on charge transfer, nonlinear capacitance, and active force associated with this protein [28–32].

In some situations, e.g., when tethers are extracted from giant vesicles, the global membrane profile can be observed optically over the course of the experiment, and these shape changes have been quantitatively depicted using models [33] based on the mechanical equilibrium equations of elastic shells [34,35]. Note that the alternative variational approach has also been used to predict the equilibrium shapes of pulled tethers [36,37]. For the OHC and HEK cell tether experiments, the membrane deformations that occur within the local region surrounding the tether have not been amenable to experimental investigation because they occur at optically irresolvable nanometer scales. Tether systems have also been studied using different experimental techniques, including recently applied standing wave fluorescence microscopy [38] and scanning electron microscopy (SEM) [39]. These deformations can also be studied by building and numerically solving a computational system that represents the important features of the physical system, which was previously done for the OHC tethers [40]. The response of the membrane to the tether's force is governed based on the mathematical equilibrium equations of elastic shells with particular constitutive equations for plasma membranes.

Computational modeling is used here to describe the detailed physical behavior of the plasma membrane in regions beyond the tether itself. The method is applied to describe the tether experiments of human embryonic kidney cells and Chinese hamster ovary cells. The simulations are based on our previously developed model for cochlear outer hair cell tether experiments. These cells all have significant membrane-cytoskeleton interactions; however, the CHO and HEK cells have different geometric substructure morphologies than the lateral walls of the OHC. The effects of each cell's cytoskeleton on the membrane, which are explicitly included here, are modeled as a linear response to the membrane's normal displacement. The microscopic regions (i.e., suboptical) of the tether experiment are described, and a detailed description of the differences and similarities of the plasma membrane's responsive behavior to tether pulling forces in these cells is presented. The approach presented here allows a better and broader interpretation of the tether pulling experiment in cells.

II. SYSTEM AND MODEL DESCRIPTION

In general, the model is used to simulate statically held membrane tethers that are pulled from unaspirated cells, and it includes an explicit representation of the region where the membrane transitions from the tether and reattaches to the cell's cytoskeleton network. It is assumed here that there is no cytoskeleton present within the tether and transition regions of the tether. The model is used here to study the effects of the magnitude of equilibrium tether holding force and the membrane's mechanical properties on the membrane's shape profiles as well as the modes of energy stored within the attachment region of the system. The simulations of the HEK and CHO cell tether experiments are based on a model that was previously developed for the cochlear outer hair cell [40]. In this section, we first provide an overview of the details of this model as it was applied to OHCs. Then we discuss all of the changes that were made to the model in order to apply it to the HEK and CHO cell cases. Finally, we provide an overview of the necessary model parameters and list all of the values used in our simulations.

A. Modeling the cochlear outer hair cell tether experiment

Under normal conditions, the outer hair cell is cylindrically shaped (radius ~ 5 μm, length ~ 15–90 μm) and has electromechanical transduction properties that allow it to contract with depolarizing potentials and elongate when hyperpolarized [41]. The outer hair cell's lateral wall is a composite structure with three main components: the plasma membrane that is directly attached to the underlying cytoskeletal lattice that sits above the subsurface cisternae (see, e.g., [42]). The activity of the protein prestin, and its interactions with the membrane lipid assembly, is transferred to the underlying cytoskeleton which results in a net active force generated by this cell. Understanding the effects of geometrical parameters as well as characterizing the mechanical properties of the OHC's plasma membrane is important toward a further understanding of the performance of this active cell under various conditions. The outer hair cell's cytoskeleton is an organized array of almost circumferential actin filaments and axial spectrin cross links [43–45]. The plasma membrane of the outer hair cell is connected to the underlying cytoskeletal actin filaments by an array of pillars of unknown molecular composition [21]. As depicted in the top panel of Fig. 2, the pillars have characteristic widths of ~ 10 nm [44] and lengths of ~ 20 nm [43], and they are typically spaced approximately 30–40 nm apart [44]. The specific nature of the membrane-pillar bond is unknown, but, as discussed previously, the bond is very strong, based on the large forces required to separate the two [21].

An illustration of the tether experiment for the OHC and HEK cell is presented in Fig. 1, with an emphasis on the spatial region that corresponds to the modeled system. The top panel illustrates the OHC case (also Fig. 1 in [40]), and the bottom panel shows the HEK cell case. As shown in Fig. 1, there are three distinct regions of the membrane: the tether region, the cytoskeleton attachment region, and the transition region that connects the tether region to the cytoskeleton attachment region. The model includes the local region sur-
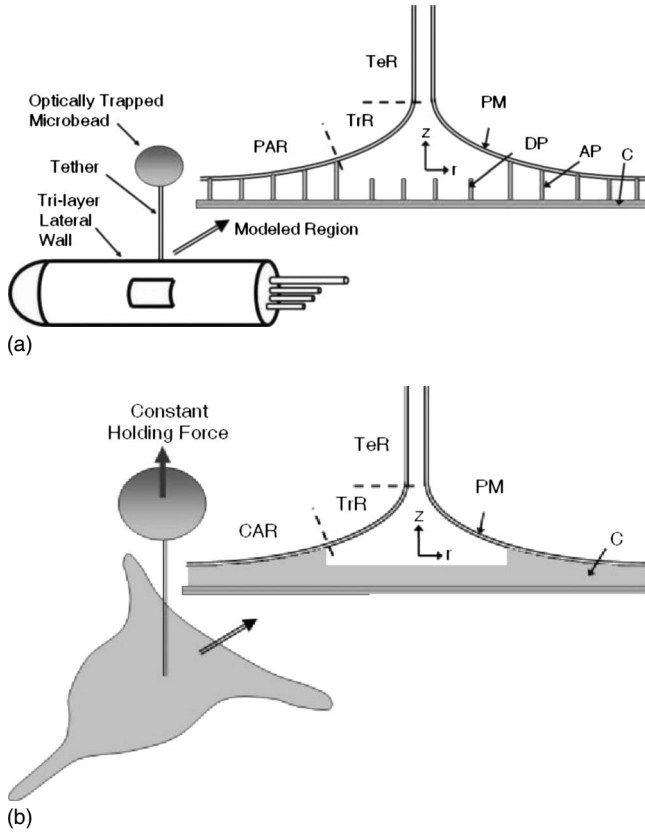
FIG. 1. Panel (a) is an illustration of the cochlear outer hair cell tether experiment, with a particular focus on the modeled region (i.e., where the membrane transitions from the tether and reattaches to the lateral wall). Panel (b) is an analogous illustration of the HEK cell tether experiment. TeR, tether region; TrR, transition region; CAR, cytoskeleton attachment region; PM, plasma membrane; DP, detached pillar; AP, attached pillar; C, cytoskeleton.

rounding the tether site, and we assume that the local system is axisymmetric with respect to the axis of the tether being held. Cylindrical coordinates (r, z, ϕ) and curvilinear coordinates (s, ψ, ϕ) may be defined, where z is the axis of symmetry, r represents the radial distance from the center of the tether, ϕ is the azimuthal angle, s is a parameter that represents the distance traveled along the meridional surface of the membrane, and ψ is the angle between the r axis and the surface normal on the membrane. The kinematic relationship equations are

$$\partial r / \partial s = \sin \psi$$

$$\partial z / \partial s = - \cos \psi,$$

and the two principal curvatures at any point on the axisymmetric surface can be written in terms of the geometric parameters ψ and r:

$$\kappa_m = - \partial \psi / \partial s$$

$$\kappa_\phi = r^{-1} \cos \psi$$

The cellular plasma membrane is modeled as a thin, two dimensional, elastic shell with internal bending moments and

shear forces. Appropriate force and moment balances on an element of the elastic shell provides the mechanical equilibrium equations for the meridional force, normal force, and moments,

$$\sigma_m r + \partial (T_m r)/\partial s - T_\phi \, \partial r/\partial s + (Q_m r) \kappa_m = 0, \quad (1)$$

$$T_m \kappa_m + T_\phi \kappa_\phi - r^{-1} \, \partial (Q_m r)/\partial s = \sigma_n, \quad (2)$$

$$r Q_m = \partial (M_m r)/\partial s - M_\phi \, \partial r/\partial s, \quad (3)$$

respectively [46]. There are two characteristic directions on the surface of the axisymmetric membrane shell, the first is the meridional direction and is designated with a subscript m, and the other is the circumferential direction and is represented by the subscript symbol ϕ. The third subscript, n, represents the outward normal direction to the surface of the membrane. Here, T represents the in-plane stress resultant, Q represents the shear stress resultant, M designates the moment resultant, σ represents an applied surface pressure related to the membrane interaction with the cytoskeleton, κ represents the curvature.

We assume that the membrane is incompressible, such that, $\varepsilon_m + \varepsilon_\phi = 0$, where ε is the strain. It is assumed that the fluidity of the membrane leads to an isotropy of the principal moment resultants, $M = M_m = M_\phi$. The constitutive equation relating the bending moment to curvatures is [47]

$$M = B(\kappa_m + \kappa_\phi). \quad (4)$$

It can be shown by integrating the principal stresses over the thickness of the membrane that

$$T_m + M \kappa_m = T_\phi + M \kappa_\phi.$$

A shooting method is used to solve the set of differential equations. The normalized differential equations that we solve are

$$\partial r' / \partial s' = \sin \psi$$

$$\partial z' / \partial s' = - \cos \psi$$

$$\partial \psi / \partial s' = - M' + r'^{-1} \cos \psi$$

$$\partial M' / \partial s' = Q'_m$$

$$\partial Q'_m / \partial s' = T'_m \kappa'_m + T'_\phi \kappa'_\phi - Q'_m r'^{-1} \sin \psi$$

$$\partial T'_m / \partial s' = (T'_\phi - T'_m) r'^{-1} \sin \psi - Q'_m \kappa'_m$$

These, along with the normalized constitutive equation, $T'_\phi + (\kappa'_\phi)^2 = T'_m + (\kappa'_m)^2$, and the curvature relations, $\kappa'_m = M' - r'^{-1} \cos \psi$ and $\kappa'_\phi = r'^{-1} \cos \psi$, form a set of closed equations.

The initial values, consisting of specified conditions within the tether (e.g., $R_t = 2\pi B / F_t$, $\psi = 0$, $Q_m = \xi$, $T_m = F_t / 2\pi R_t$, where R_t and F_t are, respectively, tether radius and holding force) are chosen and a third-order Runge-Kutta integration method is used to march along the parameter "s" in order to proceed outward along the surface meridian. The
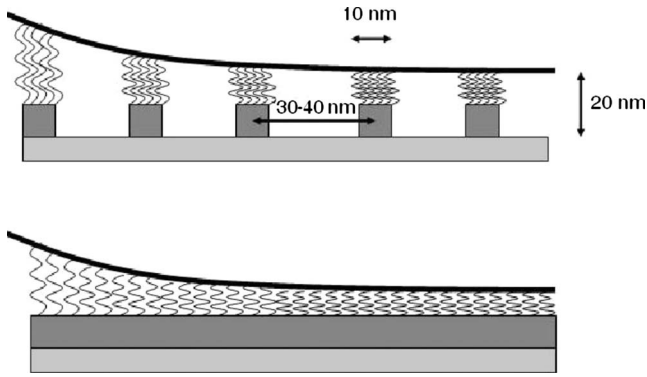
FIG. 2. Illustration of the geometries in the attachment region. The top panel represents the discrete radial pillars of the OHC; the lower panel illustrates the continuous attachment distribution of the plasma membrane to the cytoskeleton in the HEK cell. The connections between the plasma membrane and the cytoskeleton substrate are modeled as Hookean springs.

simulations proceeds until the radius equals the detachment point, and at the detachment point, the values of the moment and shear force of the obtained solution are used as boundary conditions for the attachment region. The membrane within the attachment zone is modeled as a circular plate that is attached to linear springs that represent the membrane-cytoskeleton interaction sites. We do not take into account the deformation of the substrate (cytoskeleton). The boundary conditions far from the tether are defined such that the normal deflection and the first derivative of the normal deflection are both zero. If there is a "peel off" of the membrane from the cytoskeleton, the code proceeds iteratively until the membrane has been "peeled back" a sufficient amount that the solution meets the critical displacement constraint (see further details in [40]). After calculating the shapes by solving the mechanical equilibrium equations, we calculate [Eqs. (10) and (11)] total bending energy and adhesion energy stored within the system.

In the OHC case, the discretely distributed interaction sites occur only at specific regions on the plasma membrane surface that refer to the interaction sites of the pillars, but, as described below, in the HEK cell case, the interaction sites are more evenly spread out across the entire attachment zone. When a tether is held at some force, the stresses and moments within the tether are distributed down the tether and throughout the transition region such that forces and moments are exerted on the interaction sites. The interaction sites respond to these forces by deformation, and, currently, the detailed nature of the membrane-cytoskeleton attachment is unknown. We employ a Hookean model to represent the membrane's normal reaction to force at the membrane-cytoskeleton interaction sites within the attachment zone (see Fig. 2). We assume that the connection between the membrane and cytoskeleton will fail when a critical displacement is attained. That is, if the applied force is large enough to cause the membrane to reach a critical displacement, the membrane will "peel away" from the cytoskeleton, effectively increasing the detachment zone region. The bond breakage occurs, probably, when "the head" of the bond anchored within the plasma membrane becomes removed from

its position as a result of the membrane deflection. Thus, we assume that the critical displacement of the membrane is on the order of magnitude of the membrane thickness. Below, we choose a range between 3 and 5 nm (with an average value of 4 nm) for the critical displacement of the membrane.

B. Tether modeling for the HEK and CHO cells

HEK or CHO cells are commonly used in genetic studies as a basis for plasma membrane protein transfection. For example, the electromechanical properties of prestin were studied by comparing prestin-transfected and wild-type HEK cells [28] and by investigating the electromotile capabilities of CHO cells [29]. In addition to that, HEK cells were used to investigate the structure of the prestin protein [30–32] and its prestin-related charge transfer (nonlinear capacitance) [28]. While the OHC has a regular distribution of binding sites, in the HEK and CHO cells, the plasma membrane is connected to an actin cytoskeleton by an effectively random distribution of connection sites. The identity of most of these bonds is most likely PIP2, and it is likely that there are also intramembrane proteins that help the membrane bind to the cytoskeleton. Previous studies focused on intracellular membrane-cytoskeleton adhesive properties suggest that PIP2 bonds are dynamic and can help control cellular processes such as endocytosis, cell signaling, and cell movement. Furthermore, the individual membrane-cytoskeleton bonds are locally weaker compared to the OHC pillars, but, because of their higher membrane surface concentration ($\sim$10 000 PIP2 bonds per square micron [12] vs $\sim$1000 pillars per square micron in OHCs), the integrated resultant can lead to a significant adhesive effect.

The nature and effects of a thermally fluctuating membrane in biological cells have been considered in the literature [48–51]. The thermally induced membrane undulations, characterized as a plane wave with a range of amplitudes over a frequency spectrum, can be influenced by the membrane bending modulus, the effective surface tension, as well as the complicated interaction of the membrane with the underlying cytoskeleton [49,50]. This includes the geometry of the membrane-cytoskeleton attachments such that as bond density increases, the amplitude of the fluctuations is expected to decrease. However, in our simulations of the HEK and CHO cells, we neglect the thermal membrane fluctuations that arise at molecular scales by considering only the effects of the tether force on the mean tether shape profiles.

In this section, we describe the extension of the previously described OHC tether model to apply it to HEK and CHO cells. The HEK and CHO cell tether modeling cases differ from the OHC case in the geometric treatment of the membrane-cytoskeleton bonds in the attachment region. We consider two methods of modeling the bond distribution in HEK and CHO cells: continuous and random. In the continuous approach, we assume that due to the higher density of bonds, the sites of adhesion are uniformly spread out across the surface [see Fig. 2(b)] and an effective value of the adhesion modulus is used. In the random approach, we treat the bonds as a discrete random distribution, in which we study the effects of such fine topographical details as bond width

TABLE I. Comparison of the tether formation force for various cells.

Cell Type	Tether Formation Force (pN)
Neuronal Growth Cone[a]	8
Liquid-ordered Lipid Vesicle[b]	30
Liquid-disordered Lipid Vesicle[b]	60
Chick Fibroblast[c]	35 ($n=1$)
Neutrophil[d]	45
Red Blood Cell[e]	50
Leukemic Rat Cell[f]	70
Human Embryonic Kidney Cell[g]	$246 \pm 88 (n=15)$
Outer Hair Cell (Lateral Wall)[g]	300

[a]Reference [7].
[b]Reference [8].
[c]Reference [52].
[d]Reference [53].
[e]Reference [9].
[f]Reference [3].
[g]Reference [54].

and bond spacing, parameters which affect the value of the adhesion modulus in our model.

The tether formation force is the magnitude of force required to separate the bead from the cell during the initial stage of tether formation, during which multiple membrane-cytoskeleton bonds must be broken. The tether formation force depends upon the bead size and differs for various cells, as shown in Table I. This force is interpreted to characterize the strength of bonding between the membrane and the cytoskeleton. In Table I, notice that the OHC and HEK cells have similar (large) tether formation forces relative to the other cells that are listed. Thus, based on the tether formation force, the OHC and HEK cells have an overall stronger membrane-cytoskeleton interaction than the other cells listed in Table I. We assume that, since the bead is only in contact with the membrane for a short time before tether extrusion, no focal adhesions form between the cell and the bead during initial bead contact.

In the first modeling approach, we assume that the membrane-cytoskeleton bonds in the HEK and CHO cell cases are close enough together that they can be considered as effectively continuous over the attachment region. Thus, in the continuous case, we model the bonds in the attachment zone as a continuous distribution of Hookean springs.

For the HEK cell case, we also consider the situation where the membrane-cytoskeleton bonds are randomly distributed with a typical edge-to-edge separation distance, L_{ee}, between 5 and 12 nm. The bonds themselves are estimated to have an effective bond diameter, D_b, between 3 and 10 nm. This range of bond spacing is based on the known values of typical cytoskeletal actin filament spacing in cells, and the range of bond widths is based on the typical characteristic widths of the filaments. Given a value of the average edge-to-edge bond spacing, L_{ee}, along with an estimation of the
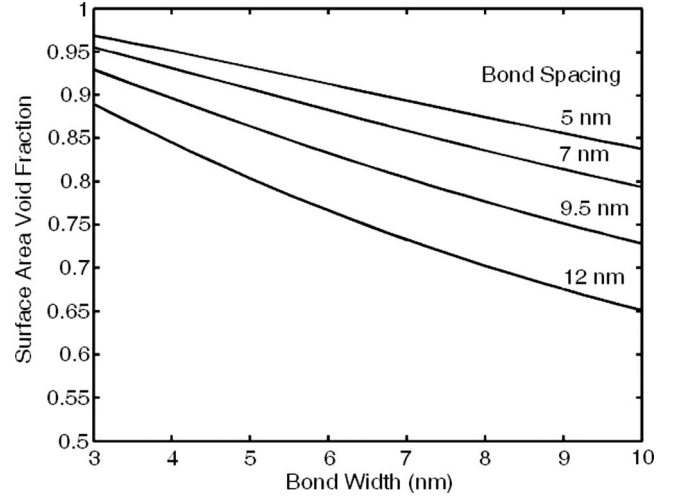

FIG. 3. Surface area void fraction as a function of bond width and edge-to-edge spacing.

average effective bond diameter, D_b, the estimated center-to-center bond spacing is then

$$L_{cc} = L_{ee} + D_b. \tag{5}$$

The bond density, ρ_P, (number of bonds per square micron) can then be estimated according to

$$\rho_P = 1/L_{cc}^2. \tag{6}$$

The bonds are distributed randomly and each realization is computed given a mean value of the edge-to-edge bond separation distance. We model the random bond separation using a Gaussian distribution function with a specified mean edge-to-edge spacing, L_{ee}, and standard deviation, $\sigma = 0.2 L_{ee}$. The details of this algorithm used to generate the random distribution are provided in Appendix A.

For a given region of membrane surface area, a certain area fraction is composed of bonds. The portion that is free from bonds is called the surface area void fraction, and can be computed as

$$\Phi = 1 - \rho_P \pi D_b^2/4. \tag{7}$$

As an illustration, Fig. 3 shows how this surface area void fraction changes as a function of bond width and edge-to-edge spacing.

In the case of discrete bonds, the model also adjusts the effective bond width with radius. Since the model assumes that the system can be represented axisymmetrically, the model's bond width parameter is corrected to ensure that the bond density and surface area void fraction remain uniform with radial distance. The details of the analysis of this effect are given in Appendix B.

C. Material and geometric parameters

1. Bending modulus

A typical range of cellular bending modulus is $10-100 k_B T$ [8]. The bending modulus for the CHO cell is obtained from Hosu *et al.* [39] to be approximately $55 k_B T$,
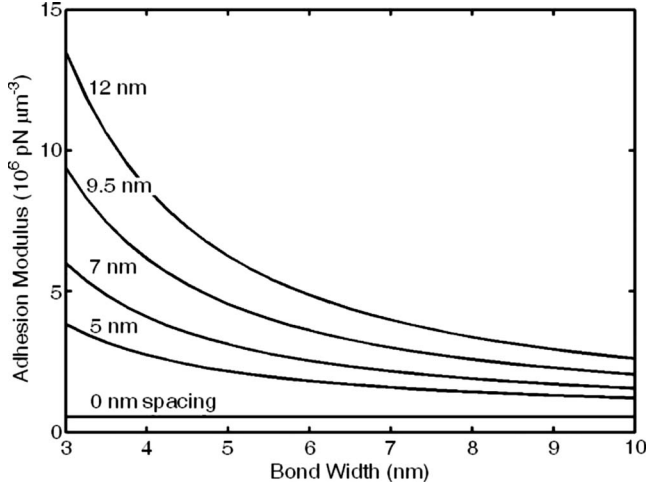
FIG. 4. Estimation of the adhesion modulus over a range of bond diameters and separation distances.

and information of particular values of this parameter for the OHC and HEK cell is not available. Note that we previously used a value of $70k_BT$ for modeling the OHC [40]. Here we include a range of bending moduli of 30, 55, and $80k_BT$, and investigate the effects on the shape profiles.

2. Adhesion modulus

In our model, the adhesion modulus is characterized by the constant k, which relates the deflection of the membrane to the normal stress. We previously estimated this modulus by using the experimental data on the tether formation force. The tether formation force for HEK cells is also available, and we use it to estimate the adhesion modulus for the HEK cell. The magnitude of the adhesion modulus corresponding to a given tether formation force depends on a particular geometry of the bond in the HEK cell. The technique of the estimation of the HEK adhesion modulus is described next, and then a variety of cases, over the range of possible parameters, are given in Fig. 4.

The critical stress required for bond breakage, $P_{P,Critical}$, is estimated based on a force balance during the initial tether breakage stage using the equation

$$P_{P,Critical} = \frac{F_{formation}}{\pi R_{d,ini}^2 \rho_P A_P},$$ (8)

where $R_{d,ini}$ is the initial radius of the detachment region, and A_p is the surface area of the cross-section of individual bond. A value of the adhesion modulus, k, is estimated according to

$$k = \frac{P_{P,Critical}}{w_{max}} = \frac{1}{w_{max}} \frac{F_{formation}}{\pi R_{d,ini}^2} \frac{1}{(1-\Phi)},$$ (9)

where w_{max} is the maximum normal extension that the membrane-cytoskeleton bonds can withstand. Thus, the bond separation distance, bond width, and critical deflection all influence the magnitude of our model parameter k.

For the HEK cell, the tether formation force is ~250 pN. If this force is distributed evenly ($L_{ee}=0$) over a detachment zone with radius 250 nm, then, using Eq. (8), the critical

pressure required to break the bonds within the detachment zone is equal to 1270 pN μm^{-2}. If we assume that the cytoskeletal substrate is rigid and that the critical deflection of the membrane is 4 nm, then, using Eq. (9), the adhesion modulus in this case is equal to $k \sim 3.2 \times 10^5$ pN μm^{-3}.

The results in Fig. 4 show that the adhesion modulus is the lowest when the bond distribution is continuous. The results also show that the adhesion modulus gets larger as the bond separation distance increases and/or the effective bond diameter gets smaller. In some instances, the adhesion modulus becomes significantly larger than the estimated value for OHC of 4.2×10^6 pN μm^{-3}.

We define the surface density of adhesion energy as $E_a = 0.5kw^2$, where w is the normal deflection of the membrane; thus, E_a is related to the total energy, E_A [Eq. (11)], via $E_A = \int E_a dA$. This adhesion energy arises as a result of interaction between the membrane, underlying actin cytoskeleton, and bond connecting the two. As an additional validation of our estimate of the HEK cell's adhesion modulus, we also derive an estimate from the measurements of the membrane-cytoskeleton interaction in cells, estimated previously based on thermodynamic analysis. One example of this approach can be found in [12], who estimated the cell's (the experiment was made in fibroblasts) surface density of adhesion energy between the membrane and the underlying actin cytoskeleton as $E_a \sim 1 \times 10^{-17}$ J μm^{-2}. A similar adhesion energy was reported in the red blood cell case was reported by Hwang and Waugh [55], $E_a \sim 6 \times 10^{-17}$ J μm^{-2}. In order to compare the adhesion energies from different sources, it is convenient to convert them into adhesion moduli. Assuming a critical average membrane deflection of 4 nm, the resulting estimate of adhesion modulus for the fibroblast is $k \sim 1.25 \times 10^6$ pN μm^{-3}, and for the red blood cell is $k \sim 7.5 \times 10^6$ pN μm^{-3}. In Fig. 4, we present a range of our estimates of the adhesion modulus determined by bond spacing and width. Thus the estimates from [12,55] obtained using thermodynamic approach fall within our range.

3. Detachment radius

When the optically trapped micro-bead separates from the cell during the initial stage of a tether pulling experiment, a number of membrane-cytoskeleton bonds are broken and a membrane-cytoskeleton detachment region is formed. The area of this initial detachment region depends on the cell-bead interfacial contact area. We assume that the tether formation force represents the force required to break the membrane-cytoskeleton bonds within the initial detachment zone. Then, we estimate the detachment area for the OHC by writing a force balance over the region and using the value of critical stress above (see Schumacher *et al.* [40] for details), and we obtain a value of $R_{d,ini}=250$ nm. For the HEK cell, we assume that the initial detachment radius is the same as that calculated for an OHC since the beads used in these experiments have the same dimensions. Note that further membrane-cytoskeleton separation may occur after the initial formation stage if tether holding forces are large enough.

TABLE II. Parameters used in the CHO cell analysis.

F_t	8 pN[a]
R_d	180 nm[b]
Bond Distribution	Continuous
R_t	72 nm[a]
B	$56k_BT$ [c]
k	3.2×10^5 pN μm^{-3}

[a]Reference [39].

[b]Estimated using Fig. 2(b) of Reference [39].

[c]B is computed using $B = R_t F_t / 2\pi$.

III. COMPUTATIONAL RESULTS AND COMPARISON WITH EXPERIMENT

A. Model validation: CHO and HEK cells

Model validation steps are important to provide confidence that a model correctly reproduces a system's experimentally measured characteristics. Using available data on CHO and HEK cells, we apply our model to simulate an individual tether pulled and held at equilibrium from these cells. The model parameters used for the CHO cell are estimated based on published data [39] and are listed in Table II. The bending modulus of $56k_BT$ was estimated using the relationship $B = R_t F_t / 2\pi$ along with the CHO cell data of $F_t = 8$ pN and measured radius of 72 nm. The detachment radius of 180 nm was estimated using the SEM image. We suppose that the membrane properties of the HEK and CHO cells are similar, and that the PIP2 and other bonds in the CHO cell are continuously distributed with an effective adhesion modulus similar to that of the HEK cell, i.e., 3.2×10^5 pN μm^{-3} (see above). In Fig. 5, the computed tether shape profiles are compared to Hosu et al.'s [39] published CHO tether image (measured using scanning electron microscopy) and Gliko et al.'s [38] published HEK tether image (measured using standing wave fluorescence microscopy).

B. Shape profiles

In this section, computational results are presented that compare some of the critical aspects of the OHC and HEK cell tether experiments. First, the computed membrane shape profiles for the OHC and HEK cell tether holding experiments, with tethers held at a constant holding force of 60 pN, are shown Figs. 6(a) and 6(b), respectively. Here, the focus is on the local regions surrounding the tether, where the membrane transitions from the tether and reattaches to the cell's cytoskeleton; note that the tether (TeR), transition (TrR), and cytoskeleton attachment (CAR) regions are labeled in the figures. For resolution purposes, Fig. 6(c) focuses on the membrane's shape within the attachment zone of each cell. Here, we use the continuous case assumption for the HEK cell.

Next, we focus on the behavior of the membrane within the cytoskeleton attachment region. In this zone, two characteristic length scales are the maximum normal deflection of
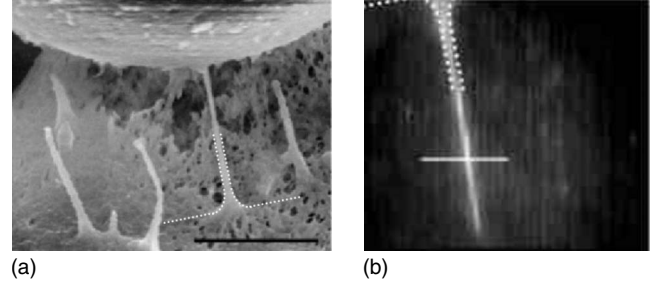

(a)   (b)

FIG. 5. Panel (a), SEM image of magnetic tweezers tether pulling experiment, where the superimposed white dotted line is our model's prediction for the shape of a tether pulled from a CHO cell. The SEM image and model parameters are based on CHO cell tether experiments by Hosu et al. Panel (b), standing wave fluorescence microscopy (SWFM) image of HEK tethers, where the white dotted line is our model's prediction of this tether's shape. The SWFM image is based on experiments by Gliko et al. Panel (a) source: B. G. Hosu, M. Sun, F. Marga, M. Grandbois, and G. Forgacs, "Eukaryotic membrane tethers revisited using magnetic tweezers," Phys. Biol. **4**, 67 (2007). Panel (b) source: O. Gliko, G. D. Reddy, B. Anvari, W. E. Brownell, and P. Saggau, "Standing wave total internal reflection fluorescence microscopy to measure the size of nanostructures in living cells," J. Biomed. Opt. **11**, 064013 (2006).

the membrane, w_{max}, and the detachment radius, R_d. Note that in all cases studied, it was observed that the (R_d, w_{max}) coordinate corresponds to the location of the detachment-attachment zone interface. Figures 7(a) and 7(b) illustrates the effects of the equilibrium holding force on w_{max} and R_d. As discussed further in the Discussion section, the oscillations in w_{max} for the OHC arise due the breaking of the discrete membrane-cytoskeleton bonds.

C. Effect of the Bending Modulus

In this section, we investigate the sensitivity of the predicted shape profiles on the magnitude of membrane bending modulus. Here, the tether holding force is 60 pN, the initial detachment radius is 250 nm, and the cytoskeletal bonding is assumed to be a continuous distribution with a critical deflection of 4 nm. Figure 8 shows the shape profiles for bending moduli of 30, 55, and $80k_BT$.

There are two primary modes of membrane free energy storage within the attachment region: the bending energy, E_B, and the membrane-cytoskeleton adhesion energy, E_A. The free energies within the attachment region are computed according to

$$E_B = 0.5B \int (\kappa_m + \kappa_\varphi)^2 dA, \qquad (10)$$

$$E_A = 0.5k \int w^2 dA, \qquad (11)$$

where the integrals are calculated over the entire surface area of the attachment region. The energies E_B and E_A are
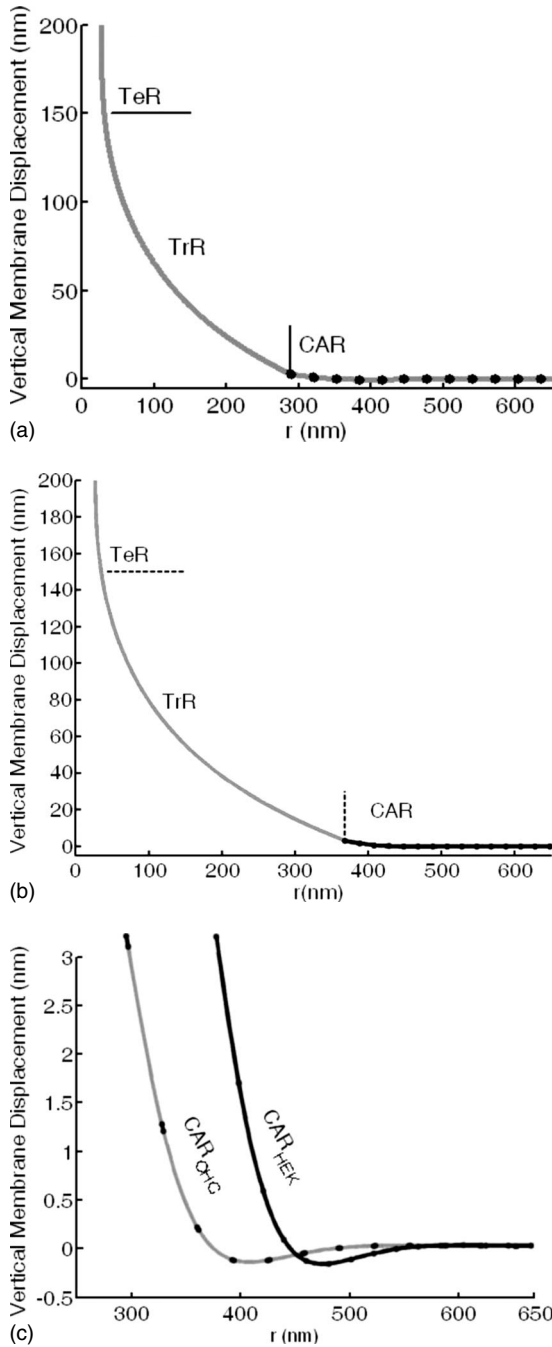
(a)

(b)

(c)

FIG. 6. The 60 pN holding force membrane shape profiles for the OHC and HEK cell. Panel (a) shows the OHC shape profile over the attachment and detachment zones; Panel (b) shows the HEK shape profile over the attachment and detachment zones; Panel (c) focuses on the attachment zone and includes the shape profile for both cells. The light-gray regions of the profile represent the spatial areas where the membrane is unattached to the cytoskeleton, and the emboldened regions of the profile represent the plasma membrane-cytoskeleton interaction sites.

computed over a range of equilibrium tether holding forces for the HEK and cases, and the results are illustrated in Fig. 9. Notice the difference in scales of the vertical axis in Panels (a) and (b).
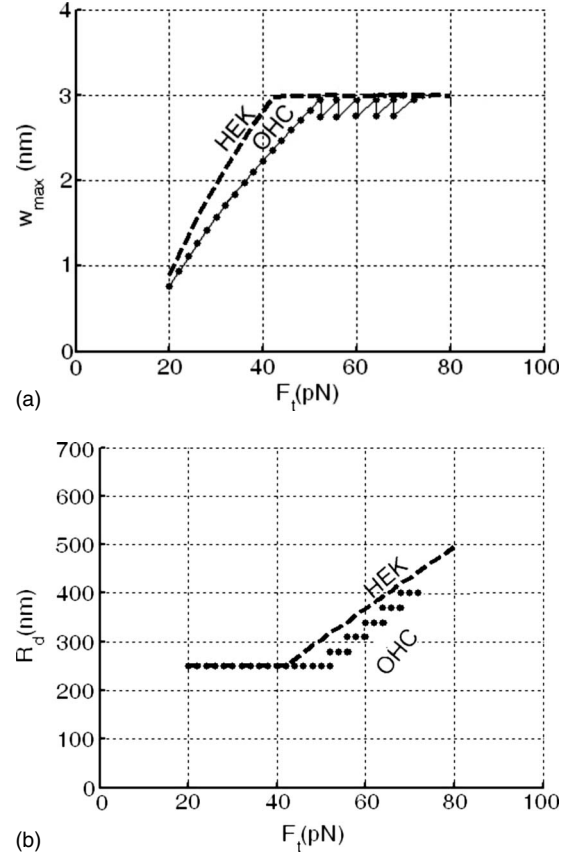

(a)

(b)

FIG. 7. Panel (a): This figure shows how the maximum deflection, within the attachment region of the cell, varies over a wide range of equilibrium tether holding forces. Panel (b): This figure shows how the detachment radius varies over a wide range of equilibrium tether holding forces.

D. Effect of the Critical Membrane Deflection

Here, we investigate the effect of another model parameter, the critical membrane deflection, which in our model influences the adhesion modulus. We assume that the tether force, initial detachment radius, and bond distribution are the same as discussed in the previous section. The bending modulus is chosen to be $55k_BT$ and the range of critical membrane deflections is 3, 4, and 5 nm. These membrane deflections correspond to adhesion moduli of $[4.24, 3.18,$ and $2.55] \times 10^5$ pN μm^{-3}, respectively. Figure 10 shows the shape profiles and Fig. 11 shows the energy modes over a range of forces.

E. Effect of the HEK cell's bond geometry

The effects of HEK cell's bond diameter and bond spacing are examined next. First, the effect of bond spacing on the shape profiles is illustrated in Fig. 12, where the geometric parameters include a constant bond diameter of 5 nm and bond spacings of 5, 7, and 9.5 nm. In Fig. 13, we plot the shape profile effects when bond spacing is set constant at 9.5 nm but variable bond widths of 5 and 10 nm are used. Figure 14 shows shape profiles when the bonds are modeled as being continuously distributed, where the two lines represent
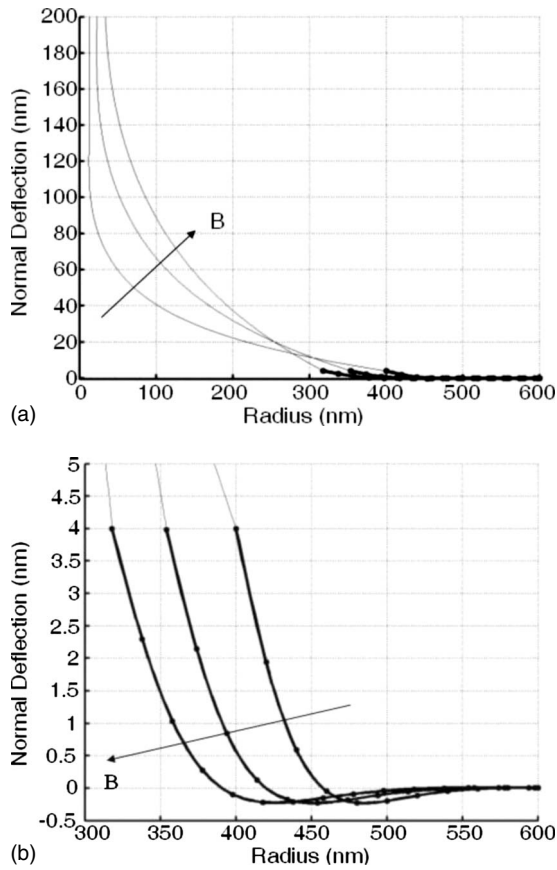
FIG. 8. Effects of varying the bending modulus on the membrane shape profile.: (a) general view and (b) attachment region. The maximum membrane deflection in the attachment region is set at 4 nm, corresponding to an adhesion modulus of 3.18 $\times 10^5$ pN μm^{-3}. The bending moduli are: 30, 55, and 80$k_B T$.

the results obtained from using different estimated values of the adhesion modulus, as described below. For each of these cases, the shape profiles are sensitive to the chosen values of these geometric parameters. Note that the adhesion modulus and surface area void fraction are estimated as described in the model section. In each case the initial detachment radius starts at 250 nm, but is usually peeled back further. We note that the continuous case seems to be a good model of the other situations with variable bond spacings and bond widths. In the cases studied, we found that the bending and adhesion energy stored within the attachment region do not significantly vary with bond width and/or bond spacing.

IV. DISCUSSION

An important consideration in membrane biophysics is the interaction of the plasma membrane with the underlying cytoskeleton. For example, if these interactions are too weak a membrane detachment may occur resulting in the formation of blebs [56], and these interactions may also be responsible for determining specific membrane domains [57]. The tether pulling experiment has been an effective tool to study cellular membrane properties. However, the membrane deformation in the attachment area is on a nanoscale and is
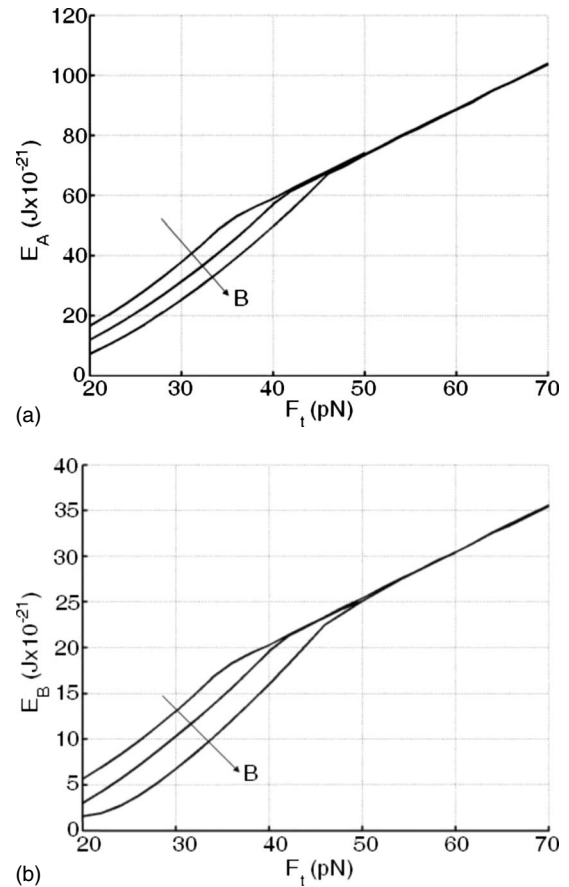

FIG. 9. This is the free energy stored within the attachment region over a range of forces. Each line is for a different bending modulus: 30, 55, and 80$k_B T$.

difficult to characterize experimentally. In previous thermodynamic-based modeling efforts, the membrane-cytoskeleton interaction was characterized by a single parameter, adhesion energy, with no explicit consideration of local geometry and density. The interpretation of the tether pulling experiment proposed in [40] and extended here includes an analysis of a geometrically detailed and place-dependent membrane-cytoskeleton interaction. We apply our interpretation of this experiment to three cells with relatively strong interaction between the membrane and cytoskeleton: the outer hair cell, the human embryonic kidney cell, and the Chinese hamster ovary cell. The first of them has a special bond topology with the membrane connected to the cytoskeleton via a system of radial pillars. The other two cells have their bond topology common to many other cells, such as fibroblasts or endothelial cells. The HEK and CHO cells are typically used in mutation/transfection studies. Simulations of the detailed shapes of membrane tethers pulled from the cochlear outer hair cell were presented in an earlier paper [40]. The membrane-cytoskeleton interaction in HEK and CHO cells probably involves bonds that connect to actin fibers. Thus, in the present study, we extend our previous model to include a more common bond topology, involving these bonds. Although these bonds are weaker than an OHC pillar, they exist in a much greater density. For example, the number of PIP2 bonds per square micron in typical cells is
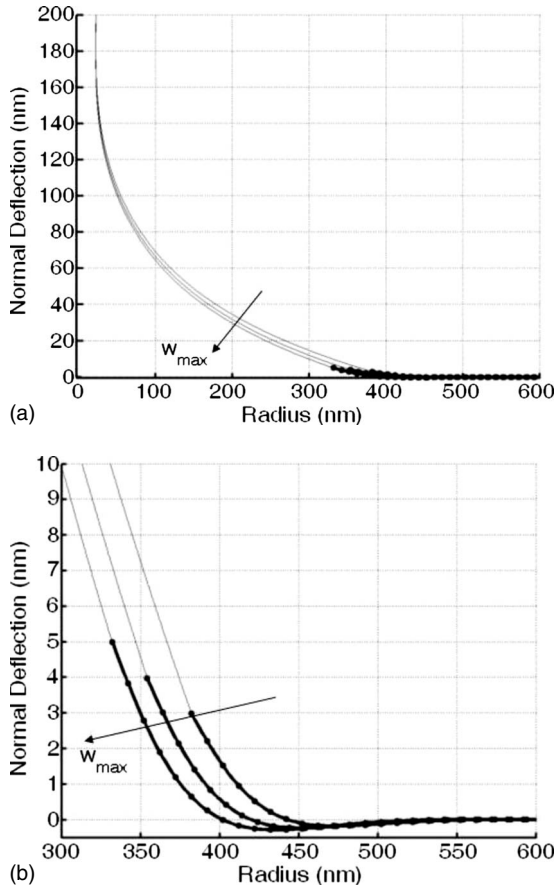
FIG. 10. Effects of varying the maximum membrane deflection in the attachment region on the membrane shape profile. The bending modulus remains constant at $55k_BT$. The values of maximum deflection in the attachment region are chosen to be 3, 4, and 5 nm, which correspond to adhesion moduli of 4.24×10^5, 3.18×10^5, and 2.55×10^5 pN μm^{-3}, respectively.

FIG. 11. Modes of free energy stored within the attachment region over a range of forces. Each line is for a different adhesion modulus: 4.24×10^5, 3.18×10^5, and 2.55×10^5 pN μm^{-3}.

about 10 000 [12] vs. fewer than 1000 for the similar pillar density in OHCs. We develop a discrete analysis of randomly distributed bonds to study the effects of bond spacing and bond widths, and this is applied to the interpretation of the tether experiment in HEK cells. Because the density of bonds may be great enough to treat them as continuously distributed, we examine the simpler continuous case using an effective adhesion modulus.

It should be noted that our model of the bond breakage in terms of the local critical membrane displacement is based on an average relative position of the membrane and the bond, while at the molecular level, the membrane and the bond statistically switch between the attachment and detachment states. We also assume that the cell cytoskeleton is much stiffer than the membrane and the bond and do not explicitly take into account the passive and active deformations of the cytoskeleton. Such cytoskeletal deformations can be implicitly taken into account via the effective density and strength of the bonds. The bond density, including that of PIP2 lipids, is important for membrane-cytoskeleton adhesion in cells. Adhesion contributes to the tether force in the membrane tether pulling experiment. Thus, the bond effect can be tested by using mutations or chemicals to reduce or
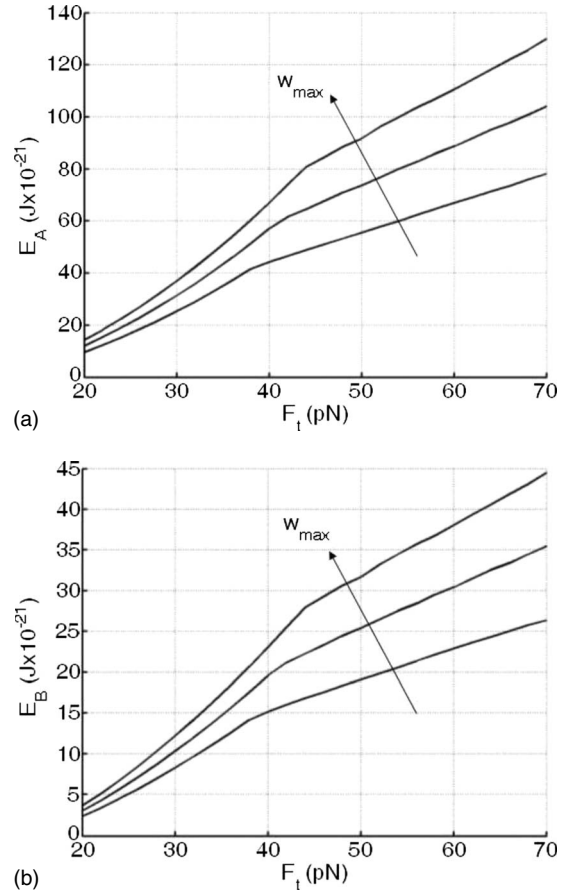
increase the corresponding membrane components and by measuring changes in the tether force caused by changes in the membrane-cytoskeleton adhesion.

For equal holding forces, the predicted behavior of the HEK, CHO, and OHC tethers are different (this is illustrated in Fig. 6 for the OHC and HEK at $F_t = 60$ pN). The difference in the response to force is due to the different bond distributions and material parameters of these cells (Table II). The HEK cell's membrane is more compliant than the OHC, due to the weaker bonds. Furthermore, there is a greater "peel off" effect (increase of the detachment zone) in the HEK cell (Fig. 6), as a result of the weaker but more numerous bonds compared to the stronger pillar bonds of the OHC.

The simulated response of each cell is studied over a range of equilibrium tether force magnitudes. The predictions show that each cell exhibits two separate types of behavior depending on the magnitude of the equilibrium tether holding force. The first occurs at lower holding forces and is characterized by a constant detachment radius and maximum deflections in the attachment region that are smaller than a critical value, 4 nm. The second takes place at larger holding forces and is characterized by an expanding detachment radius, due to the "peel off" of membrane from the cytoskeleton, and maximum deflections that are at, or near, the critical value. Based on Fig. 7, the different cells behave
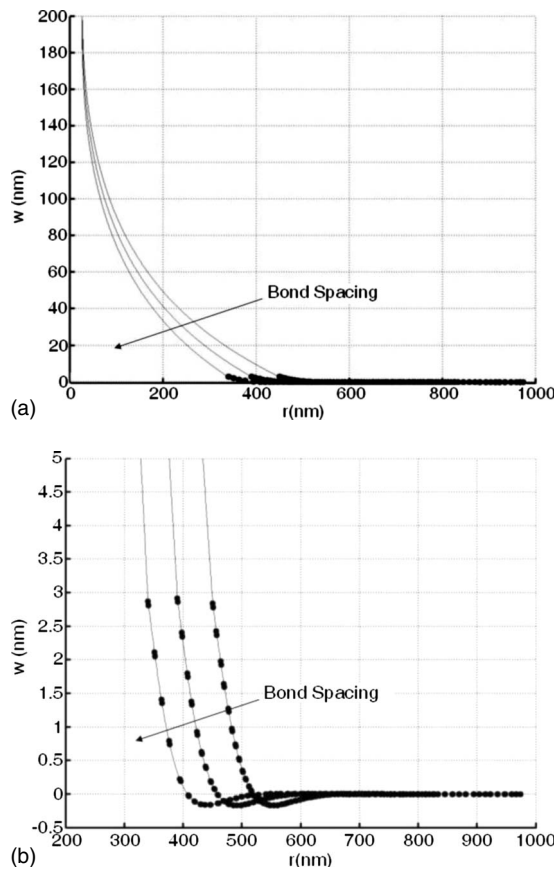
FIG. 12. Membrane shape profiles for various bond spacing in the attachment region. Bond width is constant at 5 nm. Bond spacing is 5, 7, and 9.5 nm, giving adhesion moduli of 2.2×10^6, 3.11×10^6, and 4.54×10^6 pN μm^{-3}, respectively. As bond spacing gets larger, the detachment radius gets smaller.
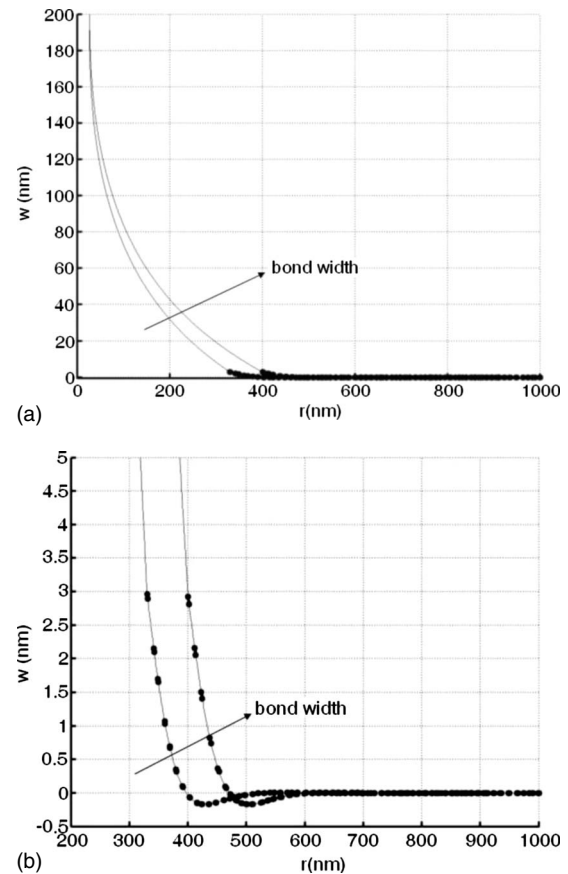

FIG. 13. Membrane shape profiles for various bond widths in the attachment region. Bond spacing is constant at 9.5 nm. Bond width is 5 and 10 nm, giving adhesion moduli of 4.54×10^6 and 2.05×10^6 pN μm^{-3}, respectively. As bond width gets wider, the detachment radius gets larger.

qualitatively similar with an approximately linear increase in maximum deflections with holding force in the lower range of holding forces. The slopes of the maximum deflection vs. force lines in this region are 0.094 and 0.067, for the HEK and OHC, respectively, and the detachment radius remains constant. In the second region of larger forces, the HEK and CHO cells respond in a qualitatively similar way, but the OHC response is different from the other two (Fig. 7). For the HEK and CHO in this range, the maximum deflection remains constant with holding force, but the detachment radius exhibits a constant, linear, "peel off" with tether holding force. For this range, the slope of the detachment radius vs. force line is 6.150 for the HEK. Due to the discrete nature of the OHC pillar bonds, the larger tether forces can cause the innermost individual pillar bonds, where the stresses are highest, to break. The model predicts that when a critical magnitude of stress is attained, the membrane can separate from the bonds closest to the tether. Further increases of the tether force leads to further membrane-bond separation. The result of breaking these discrete pillar bonds leads to the saw-tooth behavior of deflection [see Fig. 7(a)] and causes the detachment radius to increase in increments of ~40 nm [see Fig. 7(b)] rather than smoothly as in the HEK and CHO cells. This phenomenon was discussed in detail previously [40]. The effect was not captured in the light microscopy

OHC experiments ([12]) so far because it was associated with a nanometer level changes in the membrane profile. We attribute this difference between the simulated behavior of the HEK and CHO cells and the OHCs to the different types of membrane-cytoskeleton bonds present in these cells.

The membrane shape profiles (Fig. 8) are sensitive to the membrane bending modulus. In the detachment region, the shape profiles get broader as the bending modulus is increased. However, in the attachment zone, the higher bending modulus leads to a reduction in the peel off effect. In the energy analysis figure (Fig. 9), the energy in the attachment region decreases with an increase in the bending modulus. At the point of peel off, the curves converge and become linear.

According to our simulations, it may be difficult to distinguish the effects of the adhesion modulus unless the attachment region can be reasonably resolved (Fig. 10). Adjusting the maximum allowed deflection in our model, a value that affects attachment region properties, does not lead to a significant variation in the observed shape profiles. However, as shown in Fig. 11, there is a distinguishable difference in the energy modes.

Furthermore, changes in equilibrium tether force result in modulation of the free energy stored within the different regions of the system. For example, in Figs. 9 and 11, the force dependence of the bending and adhesion modes of free en-
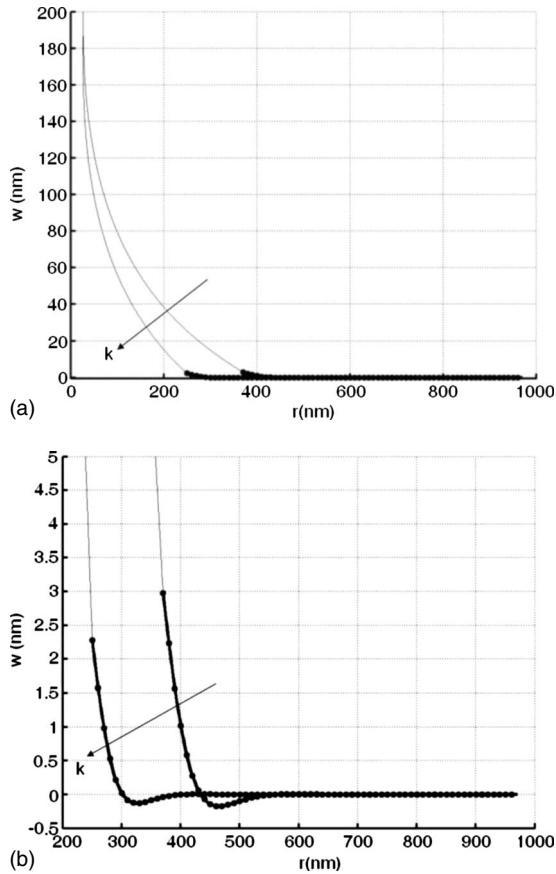
FIG. 14. Membrane shape profiles for the continuous distribution with various adhesion moduli. One case uses an adhesion modulus estimate based on HEK tether formation force (1.25×10^6 pN μm^{-3}). The other uses an adhesion modulus based on the adhesion energy value of 3.2×10^5 pN μm^{-3} from [12].

ergy is examined for the HEK cells. From these figures, our simulations predict that, in the low-force region before detachment radius expansion, the free-energy depends quadratically on the applied tether force. However, the behavior is linear for forces beyond the critical force. Note that the first derivatives of the energy functions provide information that can be used in previously developed thermodynamic incremental analyses (e.g., [2,13,55]).

For the case of the HEK cell, the model is also used to explicitly study the effects of random distributions of discrete bonds, where bond spacing and bond width were varied (Figs. 12–14). For the cases considered here, the model is constrained to ensure that the average surface density of the bonds remains spatially constant (details in Appendix). This aspect of the study is designed to mimic the effects of randomly distributed discrete bonds that have dense surface densities, particularly when compared with OHC pillar density. For the range of parameters studied, we found that as the bond spacing gets smaller (Fig. 12) or as bond width gets wider (Fig. 13) the detachment radius expands and adjusts to a larger value. The continuous-bond profiles in Fig. 14 compare the results of two different adhesion modulus estimates. Note that the continuous-bond profile (Fig. 14) based on HEK tether formation force data is a reasonable approximation to the more detailed discrete analysis. Note that the transition region's profile depends to some degree on the various bond geometries; therefore, it may be possible to determine information on these parameters by experimentally measuring the subtle changes in the detachment region's shape profile.

For the case of CHO and HEK cells, our model predicts a shape profile that is consistent with experimental SEM and standing wave fluorescence microscopy (SWFM) results for the tether, transition, and attachment regions (for the CHO), as shown in Fig. 5. Note that while the shape profile in the tether and transition regions match up well visually, the nanoscale details of the attachment region are still underresolved such that a detailed comparison in this region is not currently possible. Nevertheless, the quality of the match between our model and Hosu *et al.*'s [39] and Gliko *et al.*'s [38] experiments is encouraging, and is interpreted as an important validation step for the developed model.

In our model, we neglect the direct effects of thermal fluctuations and only consider the mean values of the variables. The attachment zone is treated as a thin annular plate with spring attachments for bonds, and the shape of this region is determined by the forces exerted on it from the tether. In the cytoskeleton region of our system, the membrane fluctuation amplitudes are expected to vary depending on the geometric bond distribution. As the bond density increases, the undulations decrease. However, directly including the effects of thermal fluctuations by including a stochastic term in the equations is beyond the scope of our current model. The effects of Brownian motion on bilayers has been investigated previously for simpler systems. For example, Brownian dynamics simulations of a mesoscopic element of an attached bilayer were performed by [58], and these simulations showed that the presence of the membrane-cytoskeleton bonds reduces the membranes thermal fluctuations relative to the pure bilayer case. Furthermore, Gov [59] theoretically predicts that the undulations also decrease with the membrane's proximity to the cytoskeleton. The effects of thermal undulations were included in a theoretical tether analyses by Glassinger and Raphael [51], who used a variational approach to show that the effective tension in a vesicle increases with tether length due to the smoothing out of membrane fluctuations. In our analysis, the tether force is balanced by the bonds as well as the effective tension in the membrane. Thus, although the undulations are not accounted for directly, the effective tension includes the effects of entropic stresses due to thermal undulations. In our model, an inclusion of thermal effects may help determine the relative contributions to the effective surface tension.

Our model predicts the membrane deflection and bending at the attachment, transition, and tether regions if the mechanical and structural parameters of the system (bending and adhesion moduli, bond width and spacing, etc.) are known. However, our approach can be used to solve inverse problems, i.e., estimation of the systems parameters if the membrane deformation can be measured. It is especially important to estimate the properties of the plasma membrane in cells with strong membrane-cytoskeleton interactions. In probing such cells' mechanical properties (e.g., with AFM or micropipette aspiration), it is often difficult to separate the membrane deformation from that of the whole cell. For ex-

ample, in our analysis of CHO cells we were able to estimate and use the bending modulus on the basis of experimentally measured tether radius and transition region. In addition to this, measurements of membrane deformation (profile) in the transition region can be used to estimate parameters of bonds connecting the membrane and the cytoskeleton. As an example, we can consider points on different curves in Figs. 12(a) and 13(a) corresponding to the same vertical displacement, w. The horizontal (r) coordinates of these points determined by bond spacing and width differ by tens of nanometers. Thus, accurate measurements [38,39] of cell's membrane profile can be used to predict the bond topology.

In the present paper, we propose a computational method to analyze, interpret, and design the tether pulling experiment in cells with a strong membrane-cytoskeleton interaction. We take into account the mechanical properties of the membrane along with the topology of the bonds connecting the membrane and the cytoskeleton. As a result, we compute the force-dependent transition and attachment zones as well as piecewise deflection, bending, and modes of stored energy in these areas. We illustrate our method by applying it to three cells: OHCs, HEKs, and CHOs, where the first of these has a special system of pillars connecting the membrane and cytoskeleton, and the other two cells have a more common arrangement via PIP2 and other bonds interacting with actin fibers. We use experimental data on tether pulling experiments in CHO cells to validate our model. The developed model can be effectively used in the analysis and interpretation of experiments aimed at probing the membrane properties in cells.

APPENDIX A: RANDOM BOND DISTRIBUTION

The probability distribution function (PDF) of the Gaussian distribution is given by

$$\text{PDF}(x) = \frac{1}{\mu\sqrt{2\pi}}\exp\left[-\frac{(x-\mu)^2}{2\sigma^2}\right], \qquad \text{(A1)}$$

and its corresponding cumulative distribution function (CDF) is

$$\text{CDF}(x) = \frac{1}{2}\left[1 + \text{erf}\left(\frac{x-\mu}{\sigma\sqrt{2}}\right)\right], \qquad \text{(A2)}$$

where μ is the mean spacing, σ is the standard deviation, and x represents the spacing. Sample illustration of the PDF and CDF functions with $\mu = 5-12$ nm and $\sigma = 2$ nm are given in Fig. 15.

The first step in the numerical generation of the randomly distributed bonds is to use a random number generator to produce a random value between 0 and 1. This value is taken to correspond to a point on the cumulative distribution func-
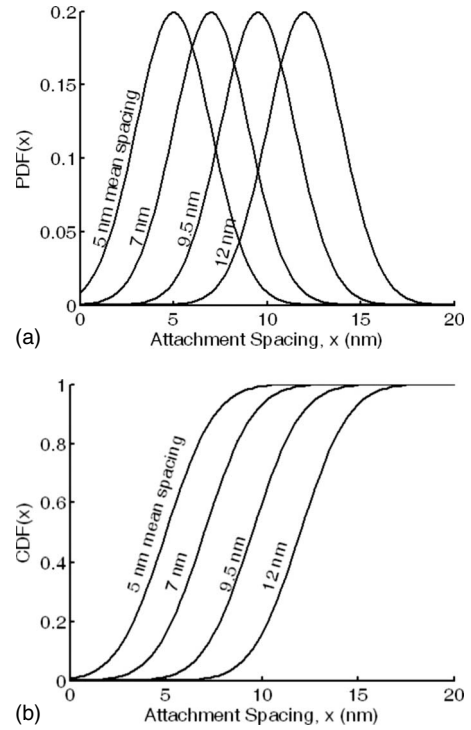

FIG. 15. An illustration of the Gaussian PDF and CDFs based on mean spacing of 5, 7, 9.5, and 12 nm and a standard deviation of 2 nm.

tion, which also ranges from 0 to 1. This random value corresponds to a specific value of the attachment spacing, x. An iterative procedure is performed to determine x such that:

$$\text{CDF}(x) - random\ number = 0.$$

This spacing x represents the edge-to-edge spacing between bond No. 1 and bond No. 2. Thus, the above steps are repeated until the spacing between every bond in the system is estimated.

As an example, say we want to generate the estimated center-to-center spacing between 21 different bonds. In this case, we take the mean spacing to be 9.5 nm and the standard deviation to be 2 nm. The results are plotted as data points Fig. 16, where the lines represent the continuous CDF and PDF functions. Notice that the majority of the attachment spacing values are between 7 and 12 nm.

APPENDIX B: EFFECTIVE BOND WIDTH

Consider an annular region of the attachment zone as depicted in Fig. 17. The gray-filled annulus represents a bond attachment site. The regions to either side of the bond attachment site represent the spaces between adjacent bonds. For example, R_i and R_o are located at the centers of interstitial spaces between bonds, and $R_{b,i}$ and $R_{b,o}$ are the inner and outer radii of the bond attachment site, respectively.

Our analysis will focus on the annular region located between the dashed lines. The total area of this annulus is
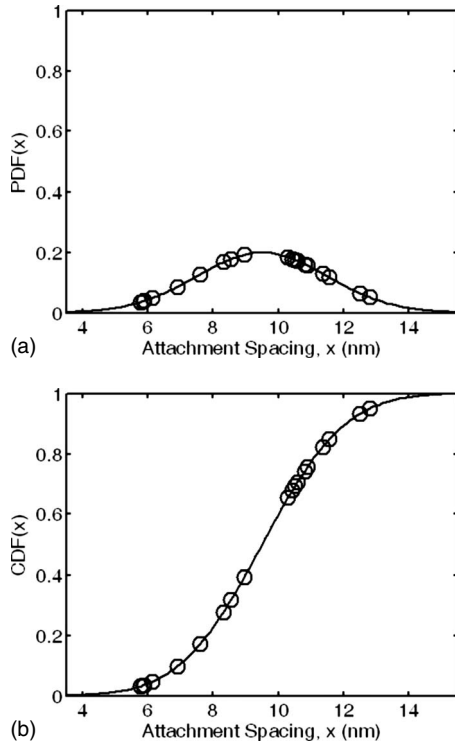
FIG. 16. The randomly generated center-to-center spacing between 21 different bonds. We take the mean spacing to be 9.5 nm and the standard deviation to be 2 nm. Data points are the edge-to-edge bond spacing value; solid line is the PDF and CDF functions.

$$A_{annulus} = \pi \lfloor R_o^2 - R_i^2 \rfloor, \qquad (B1)$$

and the area of the bond region located within this particular annulus is

$$A_{bond\ region} = \pi \lfloor R_{b,o}^2 - R_{b,i}^2 \rfloor. \qquad (B2)$$

Within this annular region, the surface area void fraction is interpreted to be equal to

$$\Phi = \frac{A_{annulus} - A_{bond\ region}}{A_{annulus}}. \qquad (B3)$$

The goal is to find the width of the bond region, $\Delta_b = R_{b,o} - R_{b,i}$, that corresponds to the specified value of Φ. The
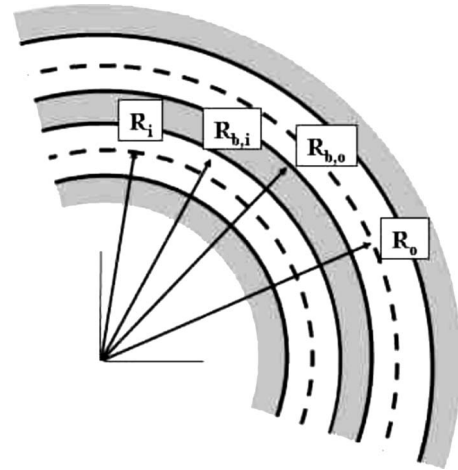

FIG. 17. Illustration of the annular spacing between bonds. The gray area represents a membrane-cytoskeleton bond site, and the white areas adjacent to the gray area represent interstitial regions between bond sites.

widths due to the bond spacing are assumed known, i.e., $\Delta_i = 2(R_{b,i} - R_i)$ and $\Delta_o = 2(R_o - R_{b,o})$. To find the bond width, the following quadratic equation must be solved for Δ_b:

$$A\Delta_b^2 + B\Delta_b + C = 0, \qquad (B4)$$

where

$$A = \Phi, \quad B = 2R_i\Phi + \Delta_o\Phi - \Delta_o, \quad C = (\Phi - 1) \cdot \lfloor \Delta_i R_i + \Delta_o R_i$$
$$+ 0.5\Delta_i\Delta_o + (0.5\Delta_i)^2 + (0.5\Delta_o)^2 \rfloor \qquad (B5)$$

As an example, consider the OHC case, which has an estimated bond density of 1100 bonds per square micron and has an estimated single bond area of $\pi 2.5 \times 10^{-5}$ square microns. The average edge-to-edge bond spacing is assumed to be 30 nm. If we take $R_i = 250$ nm, we obtain $A = 0.9136$, $B = 454.2$, and $C = -1373.8$, which gives $\Delta_b = 2.5$ nm. Note that this corrected bond diameter is approximately four times less than the actual bond diameter.

[1] R. Hochmuth, N. Mohandas, and P. Blackshear, Jr., Biophys. J. **13**, 747 (1973).
[2] L. Bo and R. Waugh, Biophys. J. **55**, 509 (1989).
[3] J. Dai and M. Sheetz, Biophys. J. **77**, 3363 (1999).
[4] Z. Li, B. Anvari, M. Takashima, P. Brecht, J. H. Torres, and W. E. Brownell, Biophys. J. **82**, 1386 (2002).
[5] C. R. Ethier and C. A. Simmonds, *Introductory Biomechanics. From Cells to Organisms* (Cambridge University Press, Cambridge, 2007).
[6] R. E. Waugh and R. M. Hochmuth, Biophys. J. **52**, 391 (1987).
[7] F. M. Hochmuth, J. Y. Shao, J. Dai, and M. P. Sheetz, Biophys. J. **70**, 358 (1996).
[8] D. Cuvelier, I. Derenyi, P. Bassereau, and P. Nassoy, Biophys. J. **88**, 2714 (2005).
[9] R. Waugh and R. Bauserman, Ann. Biomed. Eng. **23**, 308 (1995).
[10] N. Borghi and F. Brochard-Wyard, Biophys J. **93**, 1369 (2007).
[11] R. M. Hochmuth and W. D. Marcus, Biophys. J. **82**, 2964 (2002).
[12] D. Raucher, T. Stauffer, W. Chen, K. Shen, S. Guo, J. York, M.

Sheetz, and T. Meyer, Cell **100**, 221 (2000).

[13] R. Waugh, J. Song, S. Svetina, and B. Zeks, Biophys. J. **61**, 974 (1992).

[14] R. M. Raphael and R. E. Waugh, Biophys. J. **71**, 1374 (1996).

[15] G. Girdhar and J. Shao, Biophys. J. **87**, 3561 (2004).

[16] F. Brochard-Wyart, N. Borghi, D. Cuvelier, and P. Nassoy, Proc. Natl. Acad. Sci. U.S.A. **103**, 7660 (2006).

[17] M. P. Sheetz, Nat. Rev. Mol. Cell Biol. **5**, 392 (2000).

[18] M. Sheetz, J. Sable, and H. Döbereiner, Annu. Rev. Biophys. Biomol. Struct. **35**, 417 (2006).

[19] J. Zheng, W. Shen, D. Z. Z. He, K. B. Long, L. D. Madison, and P. Dallos, Nature (London) **405**, 149 (2000).

[20] M. Liberman, J. Gao, D. He, X. Wu, S. Jia, and J. Zuo, Nature (London) **419**, 300 (2002).

[21] J. S. Oghalai, A. A. Patel, T. Nakagawa, and W. E. Brownell, J. Neurosci. **18**, 48 (1998).

[22] A. Zelenskaya, J. Boutet de Monvel, D. Pesen, M. Radmacher, J. H. Hoh, and M. Ulfendahl, Biophys. J. **88**, 2982 (2005).

[23] J. A. Tolomeo and C. R. Steele, J. Acoust. Soc. Am. **97**, 3006 (1995).

[24] A. A. Spector, W. E. Brownell, and A. S. Popel, J. Acoust. Soc. Am. **103**, 1001 (1998).

[25] A. A. Spector, W. E. Brownell, and A. S. Popel, J. Acoust. Soc. Am. **103**, 1007 (1998).

[26] A. A. Spector, M. Ameen, and A. S. Popel, Biophys. J. **81**, 11 (2001).

[27] H. Wada, H. Usukura, M. Sugawara, Y. Katori, S. Kakehata, K. Ikeda, and T. Kobayashi, Hear. Res. **177**, 61 (2003).

[28] R. Zhang, F. Qian, L. Rajagopalan, F. Pereira, W. Brownell, and B. Anvari, Biophys. J. **93**, L07 (2007).

[29] J. Ludwig, D. Oliver, G. Frank, N. Klocker, A. Gummer, and B. Fakler, Proc. Natl. Acad. Sci. U.S.A. **98**, 4178 (2001).

[30] P. Dallos and B. Fakler, Nat. Rev. Mol. Cell Biol. **3**, 104 (2002).

[31] J. Meltzer and J. Santos-Sacchi, Neurosci. Lett. **313**, 141 (2001).

[32] L. Rajagopalan, N. Patel, S. Madabushi, J. Goddard, V. Anjan, F. Lin, C. Shope, B. Farrell, O. Lichtarge, and A. Davidson, J. Neurosci. **26**, 12727 (2006).

[33] C. R. Calladine and J. A. Greenwood, J. Biomech. Eng. **124**, 576 (2002).

[34] S. P. Timoshenko and S. Woinowsky-Krieger, *Theory of Plates and Shells*, 2nd ed. (McGraw-Hill, New York, 1959).

[35] W. Flugge, *Stresses in Shells* (Springer Verlag, Berlin, 1973).

[36] T. R. Powers, G. Huber, and R. E. Goldstein, Phys. Rev. E **65**, 041901 (2002).

[37] I. Derényi, F. Jülicher, and J. Prost, Phys. Rev. Lett. **88**, 238101 (2002).

[38] O. Gliko, G. Reddy, B. Anvari, W. Brownell, and P. Saggau, J. Biomed. Opt. **11**, 064013 (2006).

[39] B. Hosu, M. Sun, F. Marga, M. Grandbois, and G. Forgacs, Phys. Biol. **4**, 67 (2007).

[40] K. R. Schumacher, A. S. Popel, B. Anvari, W. E. Brownell, and A. A. Spector, J. Biomech. Eng. **130**, 31007 (2008).

[41] W. E. Brownell, C. R. Bader, D. Bertrand, and Y. de Ribaupierre, Science **227**, 194 (1985).

[42] W. E. Brownell, A. A. Spector, R. M. Raphael, and A. S. Popel, Annu. Rev. Biomed. Eng. **3**, 169 (2001).

[43] T. Arima, A. Kuraoka, R. Toriya, Y. Shibata, and T. Uemura, Cell Tissue Res. **263**, 91 (1991).

[44] A. Forge, Cell Tissue Res. **265**, 473 (1991).

[45] M. C. Holley, F. Kalinec, and B. Kachar, J. Cell Sci. **102**, 569 (1992).

[46] E. A. Evans and R. Skalak, *Mechanics and Thermodynamics of Biomembranes* (CRC Press, Boca Raton, Fla, 1980).

[47] D. C. Pamplona and C. R. Calladine, J. Biomech. Eng. **115**, 149 (1993).

[48] N. Gov, A. G. Zilman, and S. Safran, Phys. Rev. Lett. **90**, 228101 (2003).

[49] J. B. Fournier, A. Ajdari, and L. Peliti, Phys. Rev. Lett. **86**, 4970 (2001).

[50] N. Gov and S. A. Safran, Phys. Rev. E **69**, 011101 (2004).

[51] E. Glassinger and R. M. Raphael, Biophys. J. **91**, 619 (2006).

[52] D. Raucher and M. P. Sheetz, Biophys. J. **77**, 1992 (1999).

[53] J. Shao and R. Hochmuth, Biophys. J. **71**, 2892 (1996).

[54] S. A. Ermilov, D. R. Murdock, F. Qian, W. E. Brownell, and B. Anvari, J. Biomech. **40**, 476 (2007).

[55] W. C. Hwang and R. E. Waugh, Biophys. J. **74**, 3282 (1997).

[56] J. Chen and M. Wagner, Am. J. Physiol. Renal Physiol. **280**, 619 (2001).

[57] E. Luna and A. Hitt, Science **258**, 955 (1992).

[58] L. C. L. Lin and F. L. H. Brown, Biophys. J. **86**, 754 (2003).

[59] N. S. Gov, Phys. Rev. E **75**, 011921 (2007).